A&A 566, A22 (2014)
DOI: 10.1051/0004-6361/201423841

Astronomy & Astrophysics

Thermal infrared observations of asteroid (99942) Apophis with *Herschel*⋆

T. G. Müller[1], C. Kiss[2], P. Scheirich[3], P. Pravec[3], L. O'Rourke[4], E. Vilenius[1], and B. Altieri[4]

[1] Max-Planck-Institut für extraterrestrische Physik, Postfach 1312, Giessenbachstraße, 85741 Garching, Germany
e-mail: tmueller@mpe.mpg.de
[2] Konkoly Observatory, Research Center for Astronomy and Earth Sciences, Hungarian Academy of Sciences; Konkoly Thege 15-17, 1121 Budapest, Hungary
[3] Astronomical Institute, Academy of Sciences of the Czech Republic, Fričova 1, 25165 Ondřejov, Czech Republic
[4] European Space Astronomy Centre (ESAC), European Space Agency, Apartado de Correos 78, 28691 Villanueva de la Cañada, Madrid, Spain

Received 19 March 2014 / Accepted 17 April 2014

ABSTRACT

The near-Earth asteroid (99942) Apophis is a potentially hazardous asteroid. We obtained far-infrared observations of this asteroid with the *Herschel* Space Observatory PACS instrument at 70, 100, and 160 μm. These were taken at two epochs in January and March 2013 during a close-Earth encounter. These first thermal measurements of Apophis were taken at similar phase angles before and after opposition. We performed a detailed thermophysical model analysis by using the spin and shape model recently derived from applying a two-period Fourier series method to a large sample of well-calibrated photometric observations. We found that the tumbling asteroid Apophis has an elongated shape with a mean diameter of 375^{+14}_{-10} m (of an equal volume sphere) and a geometric V-band albedo of $0.30^{+0.05}_{-0.06}$. We found a thermal inertia in the range 250–800 Jm^{-2} s$^{-0.5}$ K^{-1} (best solution at Γ = 600 Jm^{-2} s$^{-0.5}$ K^{-1}), which can be explained by a mixture of low-conductivity fine regolith with larger rocks and boulders of high thermal inertia on the surface. The thermal inertia, and other similarities with (25143) Itokawa indicate that Apophis might also have a rubble-pile structure. If we combine the new size value with the assumption of an Itokawa-like density and porosity we estimate a mass between 4.4 and 6.2×10^{10} kg, which is more than 2–3 times larger than previous estimates. We expect that the newly derived properties will influence impact scenario studies and the long-term orbit predictions of Apophis.

Key words. minor planets, asteroids: individual: (99942) Apophis – radiation mechanisms: thermal – techniques: photometric – infrared: planetary systems

1. Introduction

The near-Earth asteroid 99942 Apophis was discovered in 2004 (Minor Planet Supplement 109613) and found to be on an Aten-type orbit[1] crossing the Earth orbit in regular intervals. At that time, the object raised serious concerns following the discovery that it had a 2.7% chance of striking the planet Earth in 2029[2]. Immediate follow-up observations to address these concerns took place and provided predictions that eliminated the possibility of collision in 2029, although it does enter below the orbit of the geostationary satellites at that time. However, the possibility of Apophis passing through a precise region in space (gravitational keyhole) remained, which could set it up for an impact in the mid-term future (Farnocchia et al. 2013). Apophis remains an object with one of the highest statistical chances of impacting Earth of all known near-Earth Asteroids.

The studies performed to determine the impact probability require a clear set of physical properties to understand the orbital evolution of this asteroid (Žižka & Vokrouhlický 2011; Farnocchia et al. 2013; Wlodarczyk 2013). The lack of availability of such properties (albedo, size, shape, rotation, physical structure, thermal properties) is a major limiting factor that leads to uncertainties in the role played by non-gravitational effects on that orbit. The Yarkovsky effect due to the recoil of thermally re-radiated sunlight is the most important of these non-gravitational effects.

In addition to the information on the orbit evolution, the physical properties also serve to address the possible implications if an impact were to occur. A solid body of 300 m versus a rubble pile hitting the Earth implies different levels of severity as regards its ability to pass through the atmosphere unscathed to create regional versus grand-scale damage.

Delbo et al. (2007a) determined from polarimetric observations an albedo of 0.33 ± 0.08 and an absolute magnitude of H = 19.7 ± 0.4 mag. These values led to a diameter of 270 ± 60 m, slightly smaller than earlier estimates, which were in the range 320 to 970 m, depending on the assumed albedo. Binzel et al. (2009) described the results of observations they performed in the visible to near-infrared (0.55 to 2.45 μm) of Apophis where they compared and modelled its reflectance spectrum with respect to the spectral and mineralogical characteristics of likely meteorite analogues. Apophis was found to be an Sq-class asteroid that most closely resembled LL ordinary

⋆ *Herschel* is an ESA space observatory with science instruments provided by European-led Principal Investigator consortia and with important participation from NASA.

[1] The current orbit's perihelion is at 0.746 AU, aphelion at 1.0985 AU, with a = 0.922 AU, i = 3.33°, e = 0.191.

[2] http://neo.jpl.nasa.gov/risk
http://newton.dm.unipi.it/neodys

Table 1. Observing geometries (*Herschel*-centric) and final calibrated flux densities (FD).

Julian date mid-time	λ_{ref} [μm]	FD [mJy]	FD_{err} [mJy]	r_{helio} [AU]	Δ_{obs} [AU]	α [deg]	OD/OBSID	Repetitions	Duration [s]
first visit[a] on Jan. 6, 2013:									
2 456 298.50745	70.0	36.3	1.1	1.03593	0.096247	+60.44	1333/1342258557	1–6	1928
2 456 298.50745	160.0	8.7	3.3	1.03593	0.096247	+60.44	1333/1342258557	1–6	1928
2 456 298.53059	100.0	22.8	1.7	1.03599	0.096234	+60.40	1333/1342258558	1–7	2012
2 456 298.53059	160.0	7.4	3.8	1.03599	0.096234	+60.40	1333/1342258558	1–7	2012
2 456 298.55258	70.0	37.5	1.3	1.03604	0.096221	+60.36	1333/1342258559	1–6	1730
2 456 298.55258	160.0	9.8	2.5	1.03604	0.096221	+60.36	1333/1342258559	1–6	1730
2 456 298.57455	100.0	25.0	1.5	1.03609	0.096208	+60.32	1333/1342258560	1–7	2012
2 456 298.57455	160.0	8.2	2.2	1.03609	0.096208	+60.32	1333/1342258560	1–7	2012
combined first visit:									
2 456 298.53194	70.0	36.08	0.92	1.03599	0.096233	+60.40	1342258557 + 59	all	3658
2 456 298.55394	100.0	22.56	1.17	1.03604	0.096220	+60.36	1342258558 + 60	all	4024
2 456 298.54375	160.0	9.41	1.29	1.03602	0.096226	+60.37	1342258557 ... 60	all	7682
second visit[b] on Mar. 14, 2013:									
2 456 365.77802	70.0	12.6[c]	2.7	1.093010	0.232276	–61.38	1400/1342267456	1–3	828
2 456 365.78760	70.0	11.4	2.7	1.093003	0.232307	–61.38	1400/1342267456	4–6	828
2 456 365.79719	70.0	10.4	2.7	1.092996	0.232338	–61.39	1400/1342267456	7–9	828
2 456 365.80677	70.0	12.5[c]	2.6	1.092989	0.232368	–61.39	1400/1342267456	10–12	828
2 456 365.81635	70.0	13.3[c]	2.7	1.092983	0.232397	–61.40	1400/1342267456	13–15	828
2 456 365.82594	70.0	12.4	2.6	1.092976	0.232427	–61.40	1400/1342267456	16–18	828
combined second visit:									
2 456 365.80198	70.0	11.20	1.41	1.09299	0.232352	–61.39	1400/1342267456	selected	2484
2 456 365.80198	160.0	<3.2	–	1.09299	0.232352	–61.39	1400/1342267456	all	4968

Notes. r_{helio} is the heliocentric distance, Δ_{obs} the object distance from *Herschel*, and α is the phase-angle, with negative values after opposition. OD is the *Herschel* operational day, OBSID: *Herschel* observation identifier. The repetitions specify the number of scan-maps performed and/or used to derived the given flux and error. The *Herschel*-centric apparent motions of Apophis were 205″/h (first visit in January 2013) and 58″/h (second visit in March 2013). [(a)] Light-travel time is 48.0 s; [(b)] light-travel time is 115.9 s; [(c)] Photometry is still affected by 1–2 mJy residuals from the background-elimination process, not used for the final photometry on the combined measurement.

chondrite meteorites in terms of spectral characteristics and interpreted olivine and pyroxene abundances. Binzel et al. (2009) found that composition and size similarities of Apophis with (25143) Itokawa suggested a total porosity of 40% as a current best guess for Apophis. Applying these parameters to Apophis yielded a mass estimate of 2×10^{10} kg with a corresponding energy estimate of 375 megatonnes (Mt) TNT for its potential hazard. Substantial unknowns, most notably the total porosity, allowed uncertainties in these mass and energy estimates to be as large as factors of two or three.

Up to the time of our own observations, there were no thermal infrared measurements of this asteroid. Observations from the *Spitzer* Space Telescope were not possible as Apophis was not in the *Spitzer* visibility region during the remainder of its cold mission. Moreover, because there was no close encounter with Earth between discovery and now, there are no ground-based *N*-/*Q*-band, AKARI, or WISE observations available.

We observed this near-Earth asteroid with the *Herschel* Space Observatory (Pilbratt et al. 2010) Photodetector Array Camera and Spectrometer (PACS) instrument (Poglitsch et al. 2010) at far-infrared wavelengths (Sect. 2). We present our thermophysical model analysis (Sect. 3) and discuss the results (Sect. 4).

2. Far-infrared observations with *Herschel*-PACS

The far-infrared observations with the *Herschel* Space Observatory were performed in several standard PACS mini scan-map observations in tracking mode. The observations took place on Jan. 6, 2013 (four individual observations) and on Mar. 14, 2013 (one individual observation). Each individual observation consisted of several repetitions of a mini scan-map. The observational parameters are listed in Table 1. During the first epoch all three PACS filters at 70 (blue), 100 (green), and 160 μm (red band) were used, while in the second epoch we concentrated only on the 70/160 μm filter setting because of observing-time limitations. Each measurement consisted of a mini scan-map with ten scan-legs of 3 arcmin length and separated by 4 arcsec, the scan direction was 70° (along the diagonal of the detector arrays), and the scan-speed was 20″/s. Each scan-leg was centred on the true object position at scan mid-time. The PACS photometer takes data frames with 40 Hz that are binned onboard by a factor of 4 before downlink. The total duration of our *Herschel*-PACS observations was about 2 h during the first epoch, split into four measurements of about 30 min each: 2×6 map repetitions in the blue, 2×7 map repetitions in the green band, each time with the red channel in parallel. During the second visit we only executed one single measurement of about 1.4 h, which corresponds to 18 map repetitions in the blue/red filter setting. In this case we split the data into six individual data sets with three repetitions each.

Figure 1 shows the object-centred images of the first visit in January 2013. They were produced by stacking all frames of a given band on the source position in the first frame. The background structures in these figures are not real and are related to background-source artefacts caused by the re-centring of images on the rapidly changing Apophis position. During the

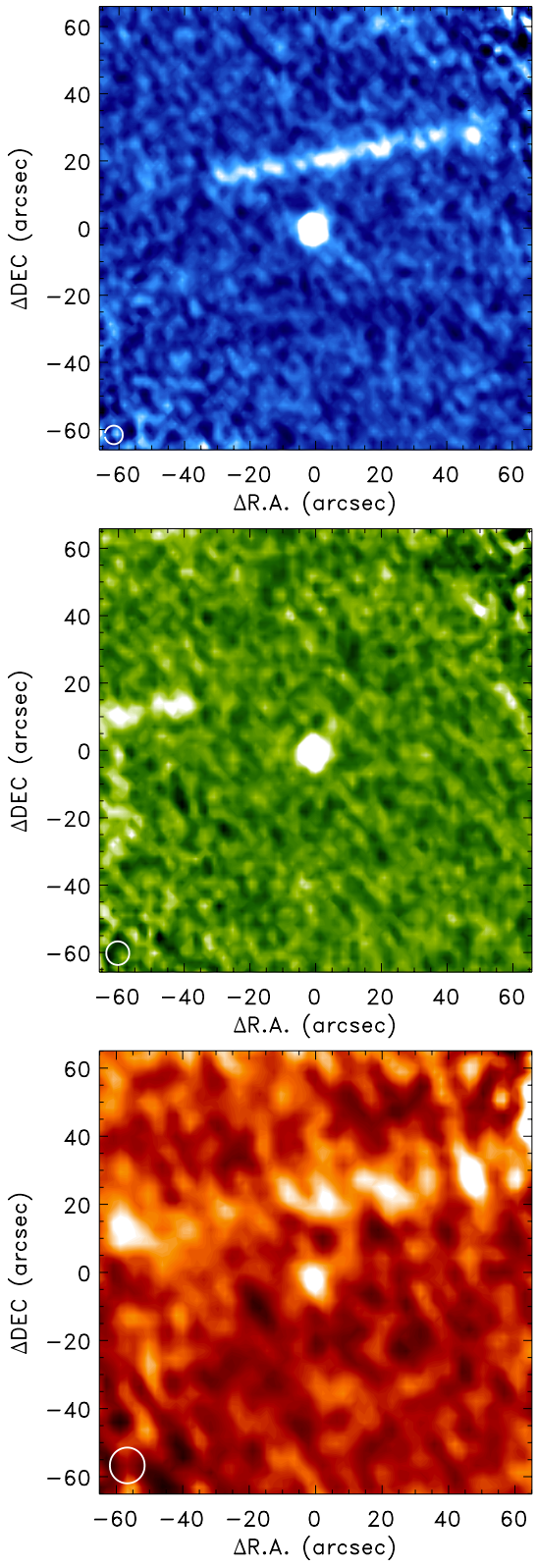

Fig. 1. Object-centred images of the target in the three PACS filters for the first visit on Jan. 6, 2013. *Top*: blue (70 μm), *middle*: green (100 μm), *bottom*: red (160 μm).

first visit Apophis was moving in a clean part of the sky without any significant sources along the object path. During the second visit the source moved across faint objects located in a field of diffuse background emission that we were not entirely able to eliminate in the reduction process. We followed the object flux (in the background-subtracted images) and noticed a 1–2 mJy residual background emission in parts of the object trajectory (see footnote in Table 1). In addition to the six sub-images, we also combined all background-free and clean images (repetitions 4–9, 16–18) to obtain a final object-centred map for high-quality photometry.

We performed aperture photometry on the final calibrated images and estimated the flux error via photometry on artificially implemented sources in the clean vicinity around our target. The fluxes were finally corrected for colour terms due to the differences in spectral energy distribution between (99942) Apophis and the assumed constant energy spectrum νF_ν = const. in the PACS calibration scheme. The calculated colour-corrections for our best Apophis model solution are 1.005, 1.023, and 1.062 at 70.0, 100.0, and 160.0 μm. These values agree with the expected corrections[3] for objects with temperatures around 250 K. The absolute flux calibration error is 5% in all three bands. This error is based on the model uncertainties of the fiducial stars used in the PACS photometer flux calibration scheme (Nielbock et al. 2013; Balog et al. 2014). Since this error is identical for all our observations, we consider it at a later stage in the discussion about the quality of our derived properties. The final monochromatic flux densities and their flux errors at the PACS reference wavelengths 70.0, 100.0, and 160.0 μm are listed in Table 1.

3. Radiometric analysis

3.1. Shape and spin properties

Pravec et al. (2014) found that Apophis has a non-principal axis rotation and is in a moderately excited short-axis mode state. The strongest observed light-curve amplitude[4] is related to a retrograde rotation with $P_1 = 30.56 \pm 0.01$ h and the angular momentum vector at $(\lambda_{\rm ecl}, \beta_{\rm ecl}) = (250°, -75°)$. The relevant parameters for our radiometric analysis are: (i) the orientation of the object at the time of the *Herschel* observations, given by the object z-axis, which is connected to the largest moment of inertia in the asteroid's co-rotating coordinate frame, and the angle ϕ_0, which specifies the rotation angle of the body at the given julian date; and (ii) the rotation history of the object to account for thermal inertia effects (the thermal inertia is responsible for transporting heat to the non-illuminated parts of the surface).

Pravec et al. (2014) were also able to reconstruct the physical shape model (see Fig. 3) of Apophis following the work by Kaasalainen (2001; 2001a) and Scheirich et al. (2010). The convex shape model with the non-principal axis rotation was determined by Pravec et al. (2014) to be the best-fit solution to the observed light curves from December 2012 to April 2013. The available photometric observations were found to cover our *Herschel* measurements in January 2013 very well. In March 2013 the situation was less favourable, and the photometric points were sparsely distributed in the days before and after the *Herschel* observations (see Fig. 6 in Pravec et al. 2014).

The light-curve-derived shape model does not have absolute size information. A dark (low albedo) and large object could explain the observed light curves equally well as a bright (high albedo) but much smaller object. For our analysis we used the

[3] PACS technical report PICC-ME-TN-038, v1.0: http://herschel.esac.esa.int/twiki/pub/Public/PacsCalibrationWeb/cc_report_v1.pdf

[4] The full (peak-to-trough) amplitude of the strongest light curve frequency $2P_1^{-1} = 2(P_\phi^{-1} - P_\psi^{-1})$ is 0.59 ± 0.03 mag, with the precession period $P_\phi = 27.38 \pm 0.07$ h and the rotation period $P_\psi = 263 \pm 6$ h.

Table 2. Apophis orientation for the nominal rotation model during the *Herschel* observations.

Julian date mid-time	z-axis [deg] λ_{ecl}	β_{ecl}	rot. angle ϕ_0 [deg]	Rotation axis [deg] λ_{ecl}	β_{ecl}
First visit on Jan. 6, 2013:					
2 456 298.50745	19.9	–58.5	243.6	234.53	–75.51
2 456 298.53059	11.5	–57.5	241.2	234.39	–75.99
2 456 298.55258	3.7	–56.4	239.3	234.44	–76.45
2 456 298.57455	356.4	–55.2	237.8	234.74	–76.92
Second visit on Mar. 14, 2013:					
2 456 365.77802	294.3	–72.9	96.2	233.35	–70.32
2 456 365.78760	293.1	–72.1	97.7	232.58	–70.53
2 456 365.79719	291.9	–71.3	99.2	231.81	–70.76
2 456 365.80677	290.6	–70.6	100.6	231.04	–71.01
2 456 365.81635	289.3	–69.8	101.9	230.38	–71.25
2 456 365.82594	287.9	–69.0	103.2	229.78	–71.49

Notes. The angular velocity was 5.00 radians/day during the first visit and 5.02 radians/day during the second visit (around the true spin axis at the given times). Numbers are given in the Apophis-centric frame.

physical shape model and the rotational properties presented in Pravec et al. (2014), the relevant coordinates and angles of our thermal measurements are listed in Table 2 and are shown in the context of a full rotation in Fig. 2.

3.2. Thermophysical model analysis

Thermophysical model (TPM) techniques are very powerful in deriving reliable sizes and albedos. When enough thermal data are available and if information about the object's shape and spin axis is available, this technique also allows one to solve for thermal properties of the surface (e.g., Harris & Lagerros 2002; Müller et al. 2005). Here the radiometric analysis was made via a thermophysical model that was based on the work by Lagerros (1996, 1997, 1998). This model is frequently and successfully applied to near-Earth asteroids (e.g., Müller et al. 2004, 2005, 2011, 2012, 2013), to main-belt asteroids (e.g., Müller & Lagerros 1998; Müller & Blommaert 2004), and also to more distant objects (e.g. Horner et al. 2012; Lim et al. 2010). The TPM takes into account the true observing and illumination geometry for each observational data point, a crucial aspect for the interpretation of our Apophis observations, which cover before- and after-opposition measurements[5]. The TPM allows one to use any available convex shape model in combination with spin-axis properties. The heat conduction into the surface is controlled by the thermal inertia Γ, while the infrared beaming effects are calculated via a surface roughness model, implemented as concave spherical crater segments on the surface and parameterised by the root mean square (rms) slope angle. We performed our radiometric analysis with a constant emissivity of 0.9 at all wavelengths, knowing that the emissivity can decrease beyond ~200 μm for some objects (e.g., Müller & Lagerros 1998, 2002), but our measurements are all at shorter wavelengths. We used a mean absolute magnitude[6] of H_V = 19.09 ± 0.19 mag, which was derived by Pravec et al. (2014) under the assumption of a slope parameter of $G = 0.24 \pm 0.11$.

[5] Before opposition: object is leading the Sun, positive phase angle in Table 1; after opposition: object is trailing the Sun, negative phase angles.

[6] The mean absolute magnitude corresponds to the mean observed cross section.

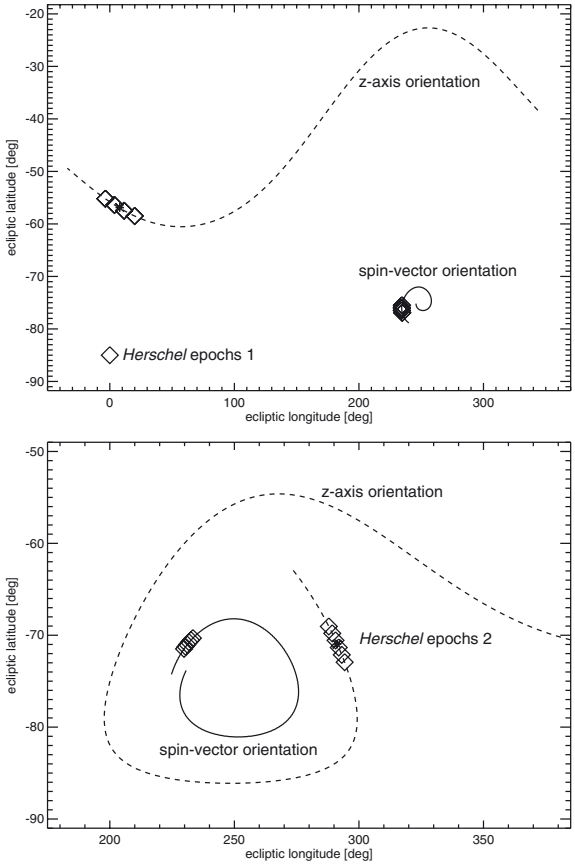

Fig. 2. Variations of the object's z-axis and spin-vector orientation during a full rotation of 30.56 h, starting about 26 h before the first *Herschel* measurement and ending about 2 h after the last measurement. The epochs of the *Herschel* observations (from Table 1) are shown as diamonts. The z axis (dashed line) is connected to the largest moment of inertia in the asteroid's co-rotating coordinate frame, the solid line shows how the orientation of the object's spin axis changes with time. *Top*: covering the first observations on Jan. 6, 2013; *bottom*: covering the second observation on Mar. 14, 2013.

3.2.1. Initial estimate for flux change due to geometry

The average observed Apophis flux at 70 μm changed from 36.7 mJy on Jan. 6 to 11.2 mJy on Mar. 14, 2013, resulting in a flux ratio FD_{epoch1}/FD_{epoch2} of 3.2. This ratio is driven by (i) the change in observing geometry (r, Δ, α); (ii) the change in cross section due to the object's non-spherical shape and the different rotational phase; and (iii) thermal effects that transport heat to non-illuminated parts of the surface.

Assuming a spherical object in instantaneous equilibrium with solar insolation (thermal inertia equals zero) would produce a very different 70 μm flux ratio FD_{epoch1}/FD_{epoch2} of 6. This calculation was the baseline for our planning of the *Herschel* observations in March (second-epoch measurement), where we expected to see approximately 6 mJy instead of the observed 11.2 mJy. The discrepancy between expectations and observations shows that changes in the observed cross section and thermal effects, in addition to the changes in observing geometry, play a significant role and are key elements for our radiometric analysis.

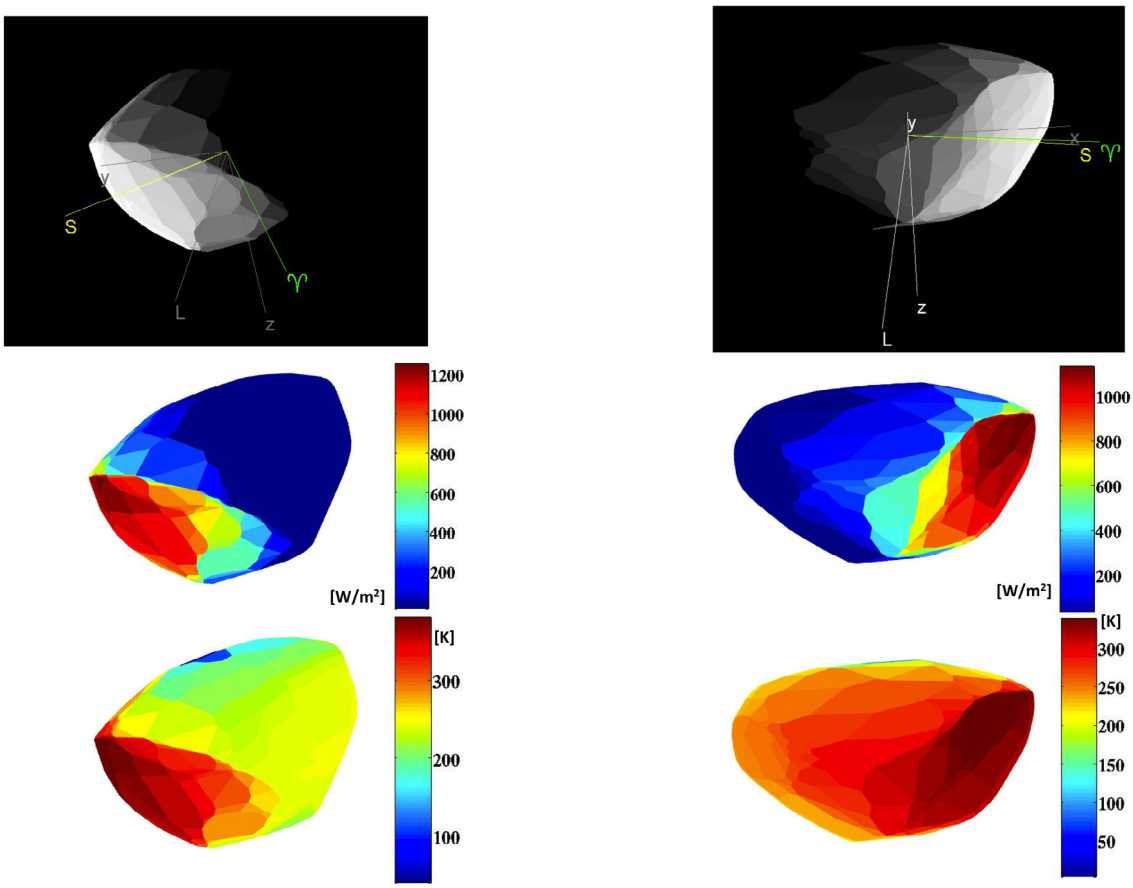

Fig. 3. Viewing geometry during the two *Herschel* observing epochs at phase angles of roughly 60° before (*left*) and after opposition (*right*). *Top*: calculated observing geometry on the basis of the nominal solution in Pravec et al. (2014). L is the fixed vector of angular momentum, the Aries sign is the x-axis of the ecliptical frame, S is the direction to the Sun, and x, y, z are the axes of the asteroid co-rotating coordinate frame (corresponding to the lowest, intermediate, and the highest moment of inertia of the body). *Middle*: the solar insolation in [W/m^2]. *Bottom*: TPM temperature calculations assuming an Itokawa-like thermal inertia of 600 Jm^{-2} s$^{-0.5}$ K^{-1}.

3.2.2. Initial estimate for flux change due to shape effects

With the availability of Apophis' shape model and rotational properties it is also possible to calculate the influence of the apparent cross section on the observed flux. Apophis was showing a 1.21 times larger cross section during the second epoch than at the first epoch. The combined geometry and cross-section change would result in a 70 μm flux ratio FD_{epoch1}/FD_{epoch2} of about 3.7, which is still significantly higher than the observed ratio of 3.2. This is a strong indication that thermal effects play an important role. The effect can also nicely be seen in Fig. 3: before opposition we see the object under a phase angle of about +60° with a cold morning terminator, while in the second epoch we see Apophis at about –61° with a warm evening side that has just rotated out of the Sun. In both cases thermal effects play a strong role: during the first epoch a substantial part of the surface heat is transported to the non-visible side, while in the second epoch the heat transport to the non-illuminated part remains visible.

3.2.3. Radiometric analysis of the first-epoch data

Figure 3 (left side) shows that the observed flux from the first epoch data taken on Jan. 6, 2013 is dominated by the illuminated/heated part of the surface and the cold morning side does not contribute in a significant manner. However, depending on the thermal inertia of the top-surface layer, there is some heat transported to the non-visible rear side. The conversion of the observed flux into a size and albedo solution depends therefore on the thermal inertia, and higher values for the thermal inertia lead to smaller size and higher albedo estimates (see Fig. 4). We applied the radiometric method to all epoch-1 data (see first part of Table 1) simultaneously and derived the size (of an equal-volume sphere) and the geometric albedo (in V band). For the calculations we used the true *Herschel*-centric observing geometry together with the correct orientation of the object at the time of the measurements (see Table 2 and Fig. 3, left side). For signal-to-noise (S/N) reasons we used the combined 100 μm flux (S/N = 19.3), the combined 160 μm flux (S/N = 7.3), and both individual 70 μm fluxes (S/N = 33.0 and 28.8). We found acceptable size-albedo solutions[7] for a wide range of thermal inertias and surface roughness settings. Only solutions connected to thermal inertias below ~250 Jm^{-2} s$^{-0.5}$ K^{-1} can be excluded because of high χ^2-values above 1.8. Figure 4 (top) shows the derived size[8] and geometric albedo values for the full range of thermal inertias. Higher values for the thermal inertia cause more heat transport to the non-visible rear side and therefore require smaller sizes to explain the observed fluxes. For the albedo there is an opposite effect, and higher thermal inertias are connected to

[7] Good-fit solutions in the sense of a weighted least-squares parameter estimation require $\chi^2_{reduced} \lesssim 1.8$ for a fit to four observational data points.

[8] The size of an equal-volume sphere.

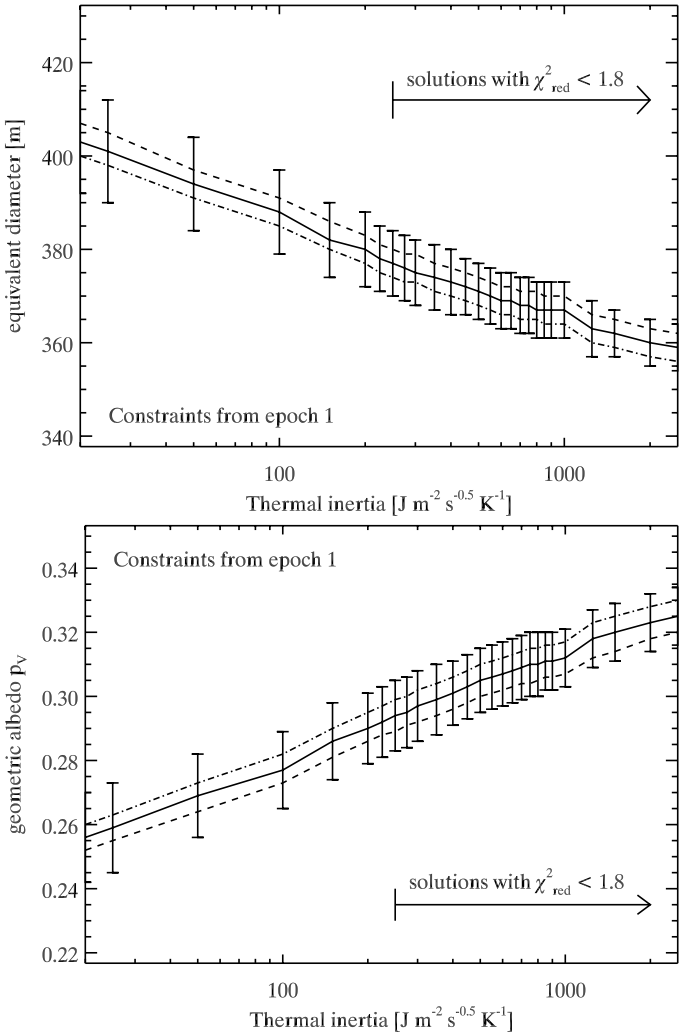

Fig. 4. Radiometrically derived size (*top*) and albedo (*bottom*) as a function of thermal inertia. The influence of model surface roughness is shown as dashed (low roughness) and dotted-dashed (high roughness) lines. The errorbars indicate the standard deviation of observation-to-model ratios for our epoch-1 measurements.

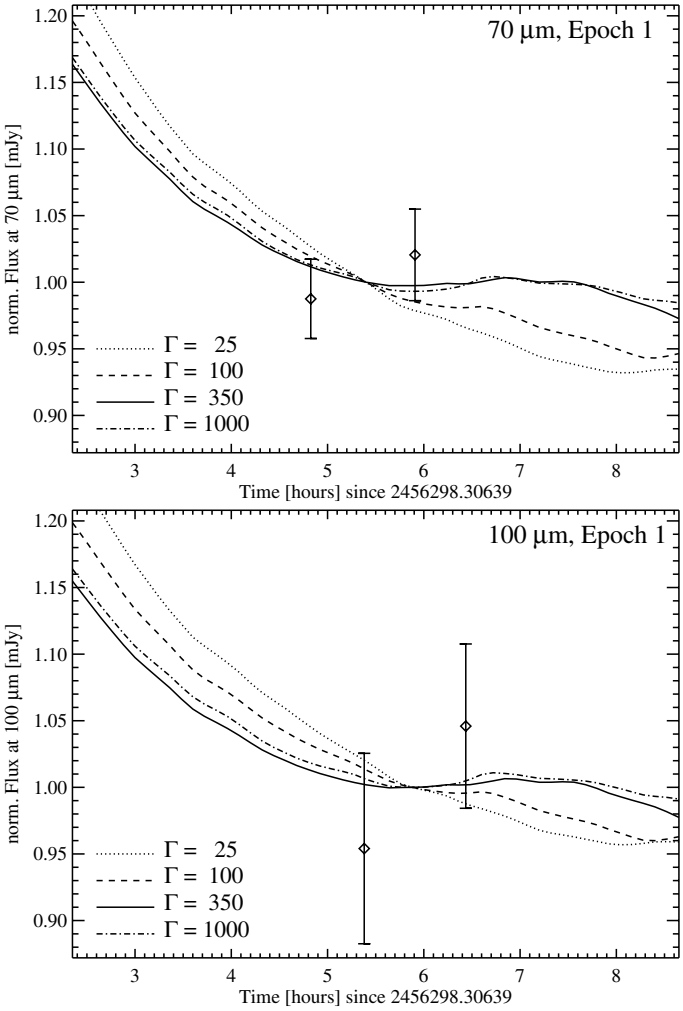

Fig. 5. TPM light curves at 70 μm (*top*) and at 100 μm (*bottom*) together with the observed fluxes and their errorbars, all normalised at mid-time. The influence of thermal inertia on the light curve is clearly visible and the measurements seem to follow the higher-inertia curves.

higher albedo values. The low influence of roughness is shown by the dashed (low rms slope angle of 0.2) and dotted-dashed (high rms slope angle of 0.9) lines. The error bars indicate the standard deviations at each thermal inertia for the size and albedo values derived from each of the four individual flux measurements. These error bars indicate the reproducibility of the result: the sizes and albedos connected to each of the independent measurements are inside the shown error bars. The 5% absolute calibration error of the PACS photometery (Balog et al. 2014) is considered below in the discussion section (Sect. 4).

The thermal inertia considerably changes the shape of the far-IR light curve at the time of our observations (see Fig. 5). At 70 μm (top) and at 100 μm (bottom) there is a flat part or even a secondary maximum developing for the higher thermal inertias. The low-thermal-inertia light curve shows a steady decrease in flux during the two hours of *Herschel* measurments. This is not seen in our time-separated observations at 70 μm and at 100 μm. The completely independent measurements in both bands seem to follow the curves for the higher thermal inertia values. At 160 μm the error bars are too large to see a similar trend. The repeated three-band high S/N measurements from Jan. 6, 2013 are therefore best fit for an object with a size of 355 to 385 m (the diameter of a sphere with the volume equal to the asteroid), a geometric albedo of 0.28 to 0.33, and a thermal inertia higher than 250 Jm^{-2} s$^{-0.5}$ K^{-1}.

3.2.4. Radiometric analysis of the second-epoch data

Figure 3 (right side) illustrates that the observed flux is influenced by the non-illuminated, but still warm part of the surface that just rotated out of the Sun. The thermal inertia influences the temperature distribution on the surface and very little heat is transported to the non-visible rear side. The conversion of the observed flux into a size and albedo solution therefore depends much less on the thermal inertia. But here we encounter some problems: (1) the S/N of the second-epoch measurement is much lower because the *Herschel*-centric distance is 2.4 times larger and because of a significant background contamination that could not be eliminated entirely (see Table 1). (2) We only obtained a single-band detection at 70 μm and an upper limit at 160 μm, but no 100 μm point was taken. (3) The coverage in optical photometric points around epoch 2 is much poorer, resulting in a less accurate model at the given orientation (see Pravec et al. 2014). The synthetic model light-curve

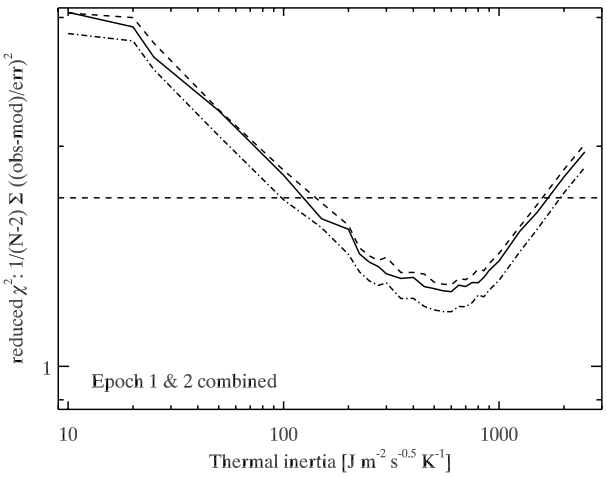

Fig. 6. Reduced χ^2-values calculated for the radiometric analysis of the combined epoch-1 and epoch-2 data set. The dashed line shows the low-roughness case, while the dashed-dotted line represents the very high roughness case. Good-fit solutions are found below the dashed horizontal line, which represents the reduced χ^2 threshold for five measurements at 1.7.

of the best-fit solution shows a local maximum on the decreasing branch, and the reliability of the calculated cross-section is unclear.

We calculated the radiometric size and albedo solutions for each thermal inertia together with the corresponding uncertainty range. The 13% error in the observed 70 μm flux translates into a 6% error in diameter and 12% error in albedo, the 160 μm detection limit unfortunately does not constrain the solution in a noticable way. As a consequence, the full range of thermal inertias is compatible with our epoch-2 data. The corresponding size and albedo values range from 370 m to 430 m and from 0.30 to 0.22, respectively.

3.2.5. Radiometric analysis of the combined data set

As a final step, we combined the radiometric results of Sects. 3.2.3 and 3.2.4 while considering the derived errors. We calculated for each thermal inertia the weighted mean size and albedo solution and used our TPM setup (including the changing orientation state of the object) to predict the flux for the four epoch-1 and one epoch-2 data points. Figure 6 shows the reduced χ^2 values together with the 1σ confidence level for five independent measurements, which is around 1.7. The three different levels of surface roughness are shown as a dashed line (ρ = 0.2, low roughness), a solid line (ρ = 0.5, intermediate roughness), and a dashed-dotted line (ρ = 0.9, very high roughness). The best solution is found at thermal inertia values of around 600 $\mathrm{Jm^{-2}\,s^{-0.5}\,K^{-1}}$, which is about mid-way inside the ~100–1500 $\mathrm{Jm^{-2}\,s^{-0.5}\,K^{-1}}$ formal acceptance range. The connected size and albedo values are 368–374 m and 0.30–0.31, respectively, with this solution being dominated by the high-quality epoch-1 data. Giving a stronger weight to the epoch-2 observations shifts the χ^2-minima to lower thermal inertias: if we weight the epoch-1 and epoch-2 solutions simply by the number of independent measurements (here 4:1), we find the χ^2-minima at a thermal inertia of around 300–350 $\mathrm{Jm^{-2}\,s^{-0.5}\,K^{-1}}$ and values higher than 800 $\mathrm{Jm^{-2}\,s^{-0.5}\,K^{-1}}$ would be excluded. The corresponding sizes are about 10 m larger and the albedo is around 0.29, but the overall match to the observations is degraded with reduced χ^2 values just below 1.7. This kind of weighting by number of observations is somewhat arbitrary, but it shows that a better balanced (higher S/N) second-epoch measurement could have influenced our results. In Sect. 4 we continue with the correct weighting of the observations taking into account the observational error bars.

4. Discussion

The radiometric method has been found to work reliably for objects whose shape and spin properties are known (e.g., O'Rourke et al. 2012 or Müller et al. 2014). The application to tumbling objects is more complex and requires the knowledge of the object orientation and its spin axis at the times of the thermal measurements. For our epoch-1 data set, the tumbling is not critical since the observed flux is clearly dominated by the illuminated part of the surface. The observed flux is not influenced by the path of the heat transport to the non-visible rear side, independent of whether the object rotates around the moment of inertia or the true spin axis. For our epoch-2 data, the situation is slightly different since the temperature distribution on the warm evening side contributes to the observed disk-integrated flux. In this case the tumbling causes a slight spatial displacement of the contributing warm region close to the terminator. It may be that our epoch-2 flux is slightly influenced by this effect and that our model predictions are therefore too low. A careful investigation showed us that the temperature of a very small region close to the rim and outside the direct Sun illumination might in reality be higher than in our TPM calculations. But the impact on the disk-integrated flux is well below 5% and the consequences for our radiometric results are negligible.

The final uncertainties of the derived size and albedo solutions mainly depend on the quality of the thermal measurements. A 10% flux error typically translates into a 5% error in equivalent size and about 10% in geometric albedo. With several independent measurements the errors can reduce to even lower values. But this is only the case when the H-magnitude is precisely known and the thermal inertia is well constrained by the available observational data set. Our data set has a good coverage in thermal wavelengths as well as phase angles before and after opposition, which is sufficient to determine the thermal inertia reliably. However, because of the problems with epoch 2, the situation is not perfect. The epoch-1 data indicate thermal inertias higher than about 250 $\mathrm{Jm^{-2}\,s^{-0.5}\,K^{-1}}$, while the combined data set excludes only the highest values above about 1500 $\mathrm{Jm^{-2}\,s^{-0.5}\,K^{-1}}$. Delbo et al. (2007b) found an average thermal inertia of 200 ± 40 $\mathrm{Jm^{-2}\,s^{-0.5}\,K^{-1}}$ for a sample of km-sized near-Earth objects with a maximum derived value of 750 $\mathrm{Jm^{-2}\,s^{-0.5}\,K^{-1}}$. We investigated the effects of very high thermal inertia values above 800 $\mathrm{Jm^{-2}\,s^{-0.5}\,K^{-1}}$ in the context of phase-angle and wavelength trends (as shown in Fig. 7). Although statistically still possible, these high values produce a trend in the observation-to-model ratios with phase angle and also cause a poor match to our most reliable 70 μm fluxes. The most likely range for the thermal inertia is therefore 250–800 $\mathrm{Jm^{-2}\,s^{-0.5}\,K^{-1}}$, with our best solution connected to 600 $\mathrm{Jm^{-2}\,s^{-0.5}\,K^{-1}}$. These high values for the thermal inertia can be explained by a mixture of (very little) low-conductivity fine regolith with larger rocks and boulders of high thermal inertia on the surface (see also discussions in Müller et al. 2012, 2013, 2014). For our best solution for the thermal inertia and a surface density of lunar regolith (1.4 $\mathrm{g\,cm^{-3}}$) together with a heat capacity somewhere between lunar regolith (640 $\mathrm{J\,kg^{-1}\,K^{-1}}$) and granite (890 $\mathrm{J\,kg^{-1}\,K^{-1}}$), the thermal conductivity κ would be 0.3–0.4 $\mathrm{W\,K^{-1}m^{-1}}$. This is compatible with Itokawa's

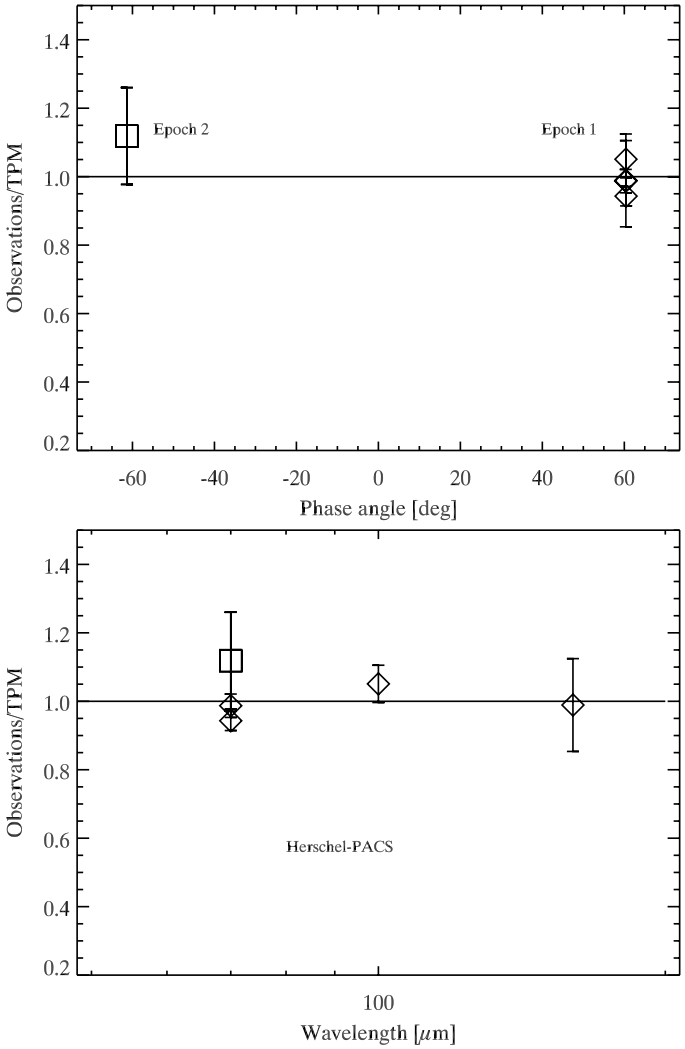

Fig. 7. Calibrated PACS observations divided by the best TPM solution as a function of phase angle (*top*) and as a function of wavelength (*bottom*).

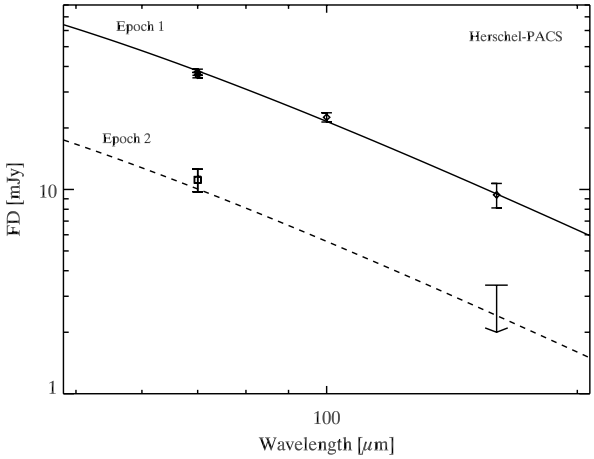

Fig. 8. Observed absolute fluxes and the corresponding TPM predictions. The best TPM solution is shown as a solid line (epoch 1) and as a dashed line (epoch 2).

0.3 $W\,K^{-1}\,m^{-1}$ (Müller et al. 2005), whereas the typical value for near-Earth asteroids is 0.08 $W\,K^{-1}\,m^{-1}$ (Mueller 2007). For the full range of uncertainties (Γ = 250–800 $Jm^{-2}\,s^{-0.5}\,K^{-1}$, heat capacity 450–1200 $J\,kg^{-1}\,K^{-1}$, and surface density 1.3–2.0 $g\,cm^{-3}$), the range for thermal conductivity would be 0.03–1.1 $W\,K^{-1}\,m^{-1}$, which is a range of two orders of magnitude.

The size range corresponding to our thermal inertia solution is 371 to 385 m (best solution 375 m) with a statistical error of only about 6 m. The smallest-radiometric-size solutions are produced by the high-roughness and high-inertia settings in the TPM, while the largest sizes are related to low-roughness/low-inertia settings (see also Rozitis & Green 2011 for a discussion on the degeneracy between roughness and thermal inertia). Since the PACS photometric system is only accurate on a 5% level (Balog et al. 2014), we have to consider it also in the context of our size solution[9]. The final size value is therefore 375^{+14}_{-10} m.

Our derived albedo range of 0.28 to 0.31 (higher values for the high-roughness, high-inertia case) has a very small statistical error below 3%. But here we have to include the influence of the absolute flux calibration (5%), as well as the H-magnitude error of ±0.19 mag, which is the dominating factor for the final solution. Overall, we find a geometric albedo solution of $0.30^{+0.05}_{-0.06}$. This value agrees well with that of Delbo et al. (2007a) of 0.33 ± 0.08, derived from polarimetric observations. The small-size solution of 270 ± 60 m by Delbo et al. (2007a) was mainly related to their H-magnitude, which is very different from the value by Pravec et al. (2014) that we used here. We can now also determine the bolometric Bond albedo A. The uncertainty in G translates into an uncertainty in the phase integral q (Bowell et al. 1989), combined with a 5% accuracy of the $q - G$ relation (Muinonen et al. 2010), we obtain a Bond albedo of $A = q \cdot p_V = 0.14^{+0.03}_{-0.04}$.

Figures 7 and 8 show our best-model solution at intermediate-roughness level in different representations. In Fig. 7 we present the observations divided by the corresponding model solutions as a function of phase angle (top) and as a function of wavelength (bottom). No trends with phase angle or wavelength can be seen. Figure 8 shows the observations and the model solution on an absolute scale. Here we also show the 160 μm upper limit from epoch 2, which agrees well with the model solution.

Binzel et al. (2009) found compositional similarities between 99942 Apophis and 25143 Itokawa. They are both are in a similar size range, have similar albedos, and similar thermal inertias. The measured density of Itokawa is 1.9 ± 0.13 g/cm^3 (Fujiwara et al. 2006; Abe et al. 2006 found a slightly higher density of 1.95 ± 0.14 g/cm^3). Using Itokawa's density and our new size estimate gives a mass estimate of $5.2^{+0.7}_{-0.6} \times 10^{10}$ kg. Both Itokawa and Apophis have been interpreted to be analogous to LL chondrite meteorites (Fujiwara et al. 2006; Binzel et al. 2009). The bulk density of meteorites of that type is 3.21 ± 0.22 g/cm^3 (Britt & Consolmagno 2003). A larger uncertainty is attached to the macro-porosity of Apophis. Britt et al. (2002) reported that asteroid macro-porosities may be up to 50%. The porosity of Itokawa is 41% (Abe et al. 2006). Assuming a porosity range of 30–50% for Apophis implies a mass between 4.4 and 6.2×10^{10} kg.

The comparison with Itokawa is interesting in many aspects: the rubble-pile near-Earth asteroid 25143 Itokawa has an effective size of 327.5 ± 5.5 m (Fujiwara et al. 2006), just 13% smaller than Apophis. Both objects have almost identical geometric albedos: 0.29 ± 0.02 for Itokawa (Bernardi et al. 2009)

[9] We added quadratically the statistical size error with a 2.5% size error related to the 5% in absolute flux calibration.

compared to $0.30^{+0.05}_{-0.06}$ for Apophis. The thermal inertias are also very similar: Müller et al. (2014) found 700 ± 200 Jm^{-2} s$^{-0.5}$ K^{-1} for Itokawa, well within the derived range for Apophis. Itokawa has a SIV-type taxonomic classification (Binzel et al. 2001) and the Hayabusa data revealed an olivine-rich mineral assemblage silimar to LL5 or LL6 chondrites (Abe et al. 2006; Okada et al. 2006). Apophis is characterised as an Sq-type that most closely resembles LL ordinary chondrite meteorites (Binzel et al. 2009). The high thermal inertia indicates a lack (or only very small amounts) of low-conductivity fine regolith on the surface. The formation of a thick regolith (typically with Γ-values below 100 Jm^{-2} s$^{-0.5}$ K^{-1}) might have been hampered by frequent seismic influence. Such processes can reorganise the body's interior and surface over short time-scales if the object has a rubble-pile structure. Apophis is also in the size range predominated by asteroids with cohesionless structures (Pravec et al. 2007). On the other hand, the density of S-type asteroids is distributed in a very narrow density interval, slightly below the density of their associated meteorites, the ordinary chondrites (Carry 2012). The macroporosity for this type of asteroids is generally lower than 30% and indicates coherent interiors, with cracks and fractures, but not rubble piles. Interestingly, the four S-type asteroids listed by Carry (2012) with sizes smaller than a few kilometres and with high-quality density information (quality codes A, B, or C) all have densities lower than 2 g cm^{-3} and a porosity of 40% or higher, which is indicative of a rubble-pile structure. Overall, the size of Apophis, its surface characteristics related to a relatively high thermal inertia, and the comparison with similar-size objects make a cohesionless structure more likely.

The newly derived properties will influence long-term orbit predictions. Chesley et al. (2003, 2008) and Vokrouhlický et al. (2008) found that the Yarkovsky effect, which is due to the recoil of thermally re-radiated sunlight, is acting on many near-Earth asteroids. It is the most significant non-gravitational force to be considered for risk-analysis studies (e.g., Giorgini et al. 2002, 2008; Chesley 2006). The calculation of the Yarkovsky orbit drift requires – in addition to the spin state, which was determined by Pravec et al. (2014) – some knowledge about the object size, bulk density, and surface thermal inertia. Our work will contribute with information about size and thermal inertia (Vokrouhlický et al., in prep.). The bulk density can be estimated from the Yarkovsky-related orbit change, which is expected to be detected by radar observations during the next close-Earth approach in September 2021 (Farnocchia et al. 2013). Žižka & Vokrouhlický (2011) showed that the solar radiation pressure also has a weak, but relevant effect on Apophis' orbit, which might be noticeable after the very close Earth encounter in 2029. Here it is mainly the size and bulk density that play a role. The combined non-gravitational forces – Yarkovsky effect and solar radiation pressure – cause small orbit drifts up to a few kilometers per decade in Apophis (Farnocchia et al. 2013). In comparison, the extension of the keyholes associated with Earth-impacts after the 2029 close encounter are in the order of 100 m or smaller. Studying the non-gravitational orbit perturbations is therefore important to estimate the distance between the true trajectory and the locations of the dangerous keyholes.

5. Conclusions

The shape and spin properties of Apophis presented by Pravec et al. (2014) were the key elements for our radiometric analysis. We interpreted the ~3.5 h of *Herschel*-PACS measurements in January and March 2013 using a well-tested and validated thermophysical model. Applying the radiometric method to a tumbling object is more complex, but it works reliably if the object orientation and its spin axis are known at the epochs of the thermal measurements. We found the following results:

1. The radiometric size solution is $D_{\rm eff} = 375^{+14}_{-10}$ m; this is the scaling factor for the shape model presented in Pravec et al. (2014) and corresponds to the size of an equal-volume sphere.
2. The geometric V-band albedo was found to be $p_V = 0.30^{+0.05}_{-0.06}$, almost identical to the value found for the Hayabusa rendezvous target 25143 Itokawa; the corresponding bolometric Bond albedo A is $0.14^{+0.03}_{-0.04}$.
3. A thermal inertia of $\Gamma = 600^{+200}_{-350}$ Jm^{-2} s$^{-0.5}$ K^{-1} best explains our combined data set that comprises three different bands and two different epochs.
4. Using either the Itokawa bulk density information or a rock density of 3.2 g/cm^3 combined with 30–50% porosity, we calculated a mass of $(5.3 \pm 0.9) \times 10^{10}$ kg, which is 2 to 3 times higher than earlier estimates.
5. No information about surface roughness can be derived from the radiometric analysis of our measurements because we lack observations at shorter wavelengths and smaller phase angles close to opposition. But the thermal inertia of Apophis is similar to the value derived for Itokawa, which might point to a surface of similar roughness.
6. The size of Apophis, the surface characteristics related to the high thermal inertia, and the comparison with similar-size objects make a cohesionless structure more likely.

The interior structure – rubble pile or coherent body – is relevant in the context of impact scenario studies. If it is a rubble-pile structure (which is the more likely option), pre-collision encounters with planets could disrupt the body by tidal forces, while a more solid interior would leave the object intact. We also expect that the newly derived properties will affect the long-term orbit predictions of Apophis, which is influenced by the Yarkovsky effect, and to second order also by the solar radiation pressure. In this context, the radiometrically derived size and thermal inertia will play a significant role in risk-analysis studies beyond the close encounter of Apophis with Earth in 2029.

Acknowledgements. We would like to thank the *Herschel* operations team, who supported the planning and scheduling of our time-constrained observations. Without their dedication and enthusiasm these measurements would not have been possible. The first-visit data are part of the *Herschel* GT1 MACH-11 project (PI: L. O'Rourke), while the second-visit data were obtained via a dedicated DDT project (PI: T. Müller). The work of P.S. and P.P. was supported by the Grant Agency of the Czech Republic, Grant P209/12/0229, by the Ministry of Education of the Czech Republic, Grant LG12001, and by Program RVO 67985815. E.V. was supported by German DLR project funding 50 OR 1108.

References

Abe, S., Mukai, T., Hirata, N., et al. 2006, Science, 312, 1344
Balog, Z., Müller, T. G., Nielbock, M., et al. 2014, Exp. Astron., accepted, DOI: 10.1007/s10686-013-9352-3
Bernardi, F., Micheli, M., & Tholen, D. J. 2009, Meteorit. Planet. Sci., 44, 1849
Binzel, R. P., Rivkin, A. S., Bus, S. J., et al. 2001, Meteorit. Planet. Sci. (Suppl.), 36, A20
Binzel, R. P., Rivkin, A. S., Thomas, C. A., et al. 2009, Icarus, 200, 480
Bowell, E., Hapke, B., Domingue, D., et al. 1989, in Asteroids II, eds. R.P. Binzel, T. Gehrels, & M. Shapley Matthews, Univ. of Arizona Press, 524
Britt, D. T., & Consolmagno, G. 2003, Meteoritics, 38, 1161
Britt, D. T., Yeomans, D., Housen, K., & Consolmagno, G. 2002, in Asteroids III, eds. W. F. Bottke Jr., A. Cellino, P. Paolicchi, & R. P. Binzel (Tucson: University of Arizona Press), 485

Carry, B. 2012, Planet Space Sci., 73, 98
Chesley, S. R. 2006, in Asteroids, Comets, Meteors, Cambridge University Press, eds. D. Lazzaro, S. Ferraz-Mello, & J. Fernández (Cambridge), 215
Chesley, S. R., Ostro, S. J., Vokrouhlický, D., et al. 2003, Science, 302, 1739
Chesley, S. R., Vokrouhlický, D., Ostro, S. J., et al. 2008, Asteroids, Comets, Meteors 2008, Baltimore, Maryland, Contribution No. 1405, Paper Id. 8330
Delbo, M., Cellino, A., & Tedesco, E. F. 2007a, Icarus, 188, 266
Delbo, M., dell'Oro, A., Harris, A. W., et al. 2007b, Icarus, 190, 236
Farnocchia, D., Chesley, S. R., Chodas, P. W., et al. 2013, Icarus, 224, 192
Fujiwara, A., Kawaguchi, J., Uesugi, K., et al. 2006, Science, 312, 1330
Giorgini, J. D., Ostro, S. J., Benner, L. A. M., et al. 2002, Science, 296, 132
Giorgini, J. D., Benner, L. A. M., Ostro, S. J., et al. 2008, Icarus, 193, 1
Harris, A. W., & Lagerros, J. S. V. 2002, in Asteroids III, eds. W. F. Bottke Jr., A. Cellino, P. Paolicchi, & R. P. Binzel (Tucson: University of Arizona Press), 205
Horner, J., Müller, T. G., & Lykawka, P. S. 2012, MNRAS, 423, 2587
Kaasalainen, M., & Torppa, J. 2001, Icarus, 153, 24
Kaasalainen, M., Torppa, J., & Muinonen, K. 2001, Icarus, 153, 37
Lagerros, J. S. V. 1996, A&A, 310, 1011
Lagerros, J. S. V. 1997, A&A, 325, 1226
Lagerros, J. S. V. 1998, A&A, 332, 1123
Lim, T. L., Stansberry, J., Müller, T. G., et al. 2010, A&A, 518, A148
Müller, T. G., & Lagerros, J. S. V. 1998, A&A, 338, 340
Müller, T. G., & Lagerros, J. S. V. 2002, A&A, 381, 324
Müller, T. G., & Blommaert, J. A. D. L. 2004, A&A, 418, 347
Müller, T. G., Sterzik, M. F., Schütz, O., et al. 2004, A&A, 424, 1075
Mueller, M. 2007, Ph.D. thesis, Freie Universität Berlin, Germany, http://www.diss.fu-berlin.de/diss/receive/FUDISS_thesis_000000002596
Müller, T. G., Sekiguchi, T., Kaasalainen, M., et al. 2005, A&A, 443, 347
Müller, T. G., Ďurech, J., Hasegawa, S., et al. 2011, A&A, 525, A145
Müller, T. G., O'Rourke, L., Barucci, A. M., et al. 2012, A&A, 548, A36
Müller, T. G., Miyata, T., Kiss, C., et al. 2013, A&A, 558, A97
Müller, T. G., Hasegawa, S., & Usui, F. 2014, PASJ, accepted [arXiv:1464.5842]
Muinonen, K., Belskaya, I. N., Cellino, A., et al. 2010, Icarus, 209, 542
Nielbock, M., Müller, T. G., Balog, Z., et al. 2013, Exp. Astron., 36, 631
Okada, T., Shirai, K., Yamamoto, Y., et al. 2006, Science, 312, 1338
O'Rourke, L., Müller, T., Valtchanov, I., et al. 2012, Planet. Space Sci., 66, 192
Pilbratt, G. L., Riedinger, J. R., Passvogel, T., et al. 2010, A&A, 518, L1
Poglitsch, A., Waelkens, C., Geis, N., et al. 2010, A&A, 518, L2
Pravec, P., Harris, A. W., Warner, B. D. 2007, in Proc. IAU Symp 236, eds. A. Milani, G. B. Valsecchi, & D. Vokrouhlický (Cambridge: Cambridge Univ. Press), 167
Pravec, P., Scheirich, P., Ďurech, J., et al. 2014, Icarus, in press
Rozitis, B., & Green, S. F. 2011, MNRAS, 415, 2042
Scheirich, P., Durech, J., Pravec, P., et al. 2010, Meteoritics, 45, 1804
Vokrouhlický, D., Chesley, S. R., & Matson, R. D. 2008, AJ, 135, 2336
Wlodarczyk, I. 2013, MNRAS, 434, 3055
Žižka, J., & Vokrouhlický, D. 2011, Icarus, 211, 511